

Enhanced diffusion barrier layers for avoiding degradation in SOFCs aged for 14000 h during 2 years

L. Bernadet^{1,*}, J. Segura-Ruiz², L. Yedra³, S. Estrade³, F. Peiró³, D. Montinaro⁴, M. Torrell¹, A. Morata^{1,*}, A. Tarancón^{1,5}

(1) IREC, Catalonia Institute for Energy Research, Dept of Advanced Materials for Energy Applications, Jardins de les Dones de Negre 1, Sant Adrià del Besòs 08930, Barcelona, Spain.

(2) ESRF, The European Synchrotron, 71 Avenue des Martyrs, Grenoble 38043, France

(3) Laboratory of Electron Nanoscopies (LENS), Micro-Nanotechnology and Nanoscopies for electrophotonic Devices (MIND), Department of Electronics and Biomedical Engineering and Institute of Nanoscience and Nanotechnology (IN2UB), University of Barcelona, C/Martí i Franquès 1, Barcelona 08028, Spain

(4) SOLIDPower SpA, Viale Trento 117, Mezzolombardo, 38017, Italy.

(5) ICREA, Passeig Lluís Companys 23, Barcelona 08010, Spain.

Tel.: + 34 933 562 615

lbernadet@irec.cat, amorata@irec.cat

Keywords

SOFC, long-term degradation, PLD diffusion barrier layer, post-mortem characterisation, YSZ-CGO interdiffusion, cathode destabilisation

Abstract

Electrolyte-cathode interfaces are critical regions of solid oxide fuel cells where important degradation phenomena are localized due to cation interdiffusion and reactivity. State-of-the-art barrier layers deposited by screen-printing are not fully blocking, resulting in the formation of insulating phases such as SrZrO₃. This article is the continuation of a previous work where a dense gadolinium doped ceria (CGO) barrier layer deposited by pulsed laser deposition (PLD) was optimized and deposited on large-area cells (80 cm²) [1]. Those cells, together with reference cells made with CGO screen-printed barrier layers were operated in the same stack for 14000 h during two years. In this work, advanced post-mortem characterisation of the cells is presented showing important microstructural differences between the two types of cell. Operated reference cells present formation of SrZrO₃ and cathode demixing, as observed in previous works. Moreover, the generation of a fracture parallel to the barrier layer inside the electrolyte is reported, which is compatible with the coalescence of Kirkendall voids formed at the diffusion front of the Gd/Ce cations into the electrolyte. In contrast, the PLD barrier layer remains stable, avoids the formation of insulating phases and prevents the formation of the mentioned fracture.

Introduction

Solid Oxide Fuel Cells (SOFCs) are efficient electrochemical devices able to convert renewable hydrogen into electricity, which makes them promising candidates to play a major role in the energy transition from fossil fuels to renewable energies. Massive deployment of this technology relies on its capacity to operate with high efficiencies and low degradation rates for hundreds of thousand hours. In this regard, elevated temperatures employed during the manufacturing of SOFC cells (comprised between 1000 and 1500 °C) and operation under harsh conditions (high temperature, strong polarisation and extremely reducing/oxidising atmospheres [2]) are primary sources of degradation. In particular, one source of performance decrease comes from the reaction between commonly used cathodes such as $\text{La}_{1-x}\text{Sr}_x\text{Co}_{1-y}\text{Fe}_y\text{O}_{3-\delta}$ (LSCF) mixed ionic-electronic conductors with the state-of-the-art electrolytes based on yttria-stabilised zirconia (YSZ). It results in the formation of insulating secondary phases such as strontium zirconate (SrZrO_3) and lanthanum zirconate ($\text{La}_2\text{Zr}_2\text{O}_7$) and the decomposition of the cathode material [3–5]. According to previous works, this reaction takes place during the cell manufacturing at high temperature and during continuous operation at intermediate temperature [6,7]. The addition of an interlayer between the electrolyte and the cathode, usually made of $\text{Ce}_{1-x}\text{Gd}_x\text{O}_{2-\delta}$ (CGO), limits the formation of those secondary phases [8]. However, a complete protection against this reaction is hardly obtained for the state-of-the-art barrier layers fabricated with screen-printing, mainly due to the elevated porosity typically obtained [9]. This poor densification of the barrier layer is mainly due to the limitation in the maximum sintering temperature imposed by the interdiffusion of CGO and YSZ, which forms an interlayer with lower ionic conductivity at temperatures above 1200 °C [10–12]. Matsui et al. studied such CGO-YSZ solid solutions demonstrating that low-conductive regions resulting from the CGO/YSZ interdiffusion tend to expand upon cathodic polarisation, which introduces significant resistances in the final device [11,13]. On the other hand, porous barrier layers are partly efficient since they prevent the formation of a continuous layer of SrZrO_3 . In this regard, Morales et al. showed that the formation of SrZrO_3 was predominantly occurring at the grain boundaries and inside the pores [14]. According to the authors, this was happening especially during the manufacturing process, as no significant changes were observed across the barrier layer after 3000 h of operation in SOFC configuration. Regarding the effect of long-term operation on the oxygen electrode and barrier layer region, Monaco et al. have recently studied this phenomenon by synchrotron X-ray micro-diffraction and micro-fluorescence on samples aged for 1800 h in solid oxide electrolysis cell (SOEC) and 15000 h in SOFC [15]. They observed an increase of the LSCF destabilization resulting in SrZrO_3 formation and an increase of the CGO/YSZ interdiffusion under higher operating temperature (850 °C vs. 750 °C) and favoured in anodic polarisation.

In order to prevent the appearance of secondary phases and low-conductive regions between the electrolyte and the cathode, strategies are being employed to densify the barrier layer without increasing its sintering temperature, such as the use of sintering aids [16] and low-temperature deposition methods such as spray pyrolysis [17] or spin coating of a hydrogel solution [18]. Alternatively, physical deposition techniques such as magnetron sputtering [6,19–21], Electron Beam Physical Vapour Deposition (EB-PVD) [6,22] and Pulsed Laser Deposition (PLD) [1,8,23–25] represent promising alternatives to fabricate dense and thin barrier layers at lower temperatures. Despite reaching fully dense layers, formation of SrZrO_3

had been reported due to the strong Sr- and Zr-diffusivity along the high number of grain boundaries typically present in deposited thin films. To solve this, an annealing step of the deposited layers at moderate temperatures has been successfully implemented, leading to a remarkable grain growth that virtually removes any diffusion pathway [1,26,27]. Regarding PVD barrier layers, only few studies present degradation measurements for a maximum of 1500 h [8,23,26,28,29]. Riegraf et al. found that a CGO barrier layer made by EB-PVD with a minimum thickness of 0.5 μm could avoid the formation of SrZrO_3 on electrolyte-supported cells after fabrication and operation in SOFC mode for 840 h [22]. By employing PLD barrier layers, Knibbe et al. found that the increase of ohmic resistance observed after 1500 h at 0.75 $\text{A}\cdot\text{cm}^{-2}$ in cathodic polarisation was not related to the SrZrO_3 detected around the PLD barrier layer that had been formed during the cell manufacturing [8]. An increase of performance above 70 % at 750 $^\circ\text{C}$ compared to state-of-the-art (SoA) cells made with screen-printed barrier layer was obtained by Morales et al. after optimizing the deposition conditions (600 $^\circ\text{C}$) and the annealing temperature (1150 $^\circ\text{C}$) of a CGO barrier layer deposited by PLD [1]. They managed to limit the Sr and Zr inter-diffusion happening during the cell manufacturing steps, leading to the reduction of the cell serial resistance. Those promising results obtained at button cell scale were up-scaled to large area cells and an aging of 4500 h in SOFC realistic operating conditions was still ongoing at the publication time.

This work makes a step forward, evaluating for the first time the long-term durability of enhanced CGO barrier layers produced by physical methods in large-area SOFC cells of 80 cm^2 . Three cells with barrier layers deposited by pulsed laser deposition were fabricated following previously optimized conditions [1], and were operated in SOFC mode for 14000 h. In order to evaluate the impact of this type of interlayers onto the cell degradation, three reference cells made with a screen-printed barrier layer were also subjected to the long-term operation in the very same stack. We present a comprehensive post-mortem analysis of all these operated cells compared to two pristine reference cells made in identical conditions by PLD and by standard screen-printing procedure. Post-mortem characterisations have been conducted by a complementary set of advanced characterization techniques with nanometric resolution and mapping capabilities. In particular, nano-X-Ray fluorescence (XRF) was employed to determine chemical composition of the cross-section of the cells with nanoscale precision; micro-Raman Spectroscopy was used to provide complementary information about the presence of secondary phases all along the interfaces; and Transmission Electronic Microscopy (TEM) was performed to reach out composition and crystal structure at the nanoscale.

Experimental methods

Cells fabrication

Two types of large-area cells with different barrier layers were fabricated. The cells consisted in a Ni-YSZ porous cermet of 260 μm and a dense 8YSZ (ZrO_2 stabilised with 8 mol.% of Y_2O_3) electrolyte manufactured by aqueous tape-casting and co-sintered at 1400 $^\circ\text{C}$.

A CGO barrier layer was deposited on top of each cell by two different techniques. On the one hand, standard screen-printing technique was used to deposit a layer of $\text{Ce}_{0.9}\text{Gd}_{0.1}\text{O}_{2-\delta}$ and then sintered at ca. 1300 $^\circ\text{C}$. Screen printing inks were formulated by mixing the ceramic powders with a vehicle composed of terpineol and ethylcellulose and the mixture was homogenised by triple roll milling. After screen printing, the solvent was evaporated by heating the samples in an oven at 70 $^\circ\text{C}$ for 10 minutes. On the other hand, a dense $\text{Ce}_{0.8}\text{Gd}_{0.2}\text{O}_{2-\delta}$ barrier layer was deposited on top of the dense electrolyte by PLD technique using a PVD5000 system (PVD Products) designed for large-area samples (up to 12 cm) and able to host four targets of up to 10 cm. The distance between the sample and the target was set to 90 mm and the deposition took place at 600 $^\circ\text{C}$ with an energy reaching the target of 200 mJ and an oxygen pressure in the chamber of 20 mTorr. An annealing process was then realized at 1150 $^\circ\text{C}$ for 2 h. Further details about the PLD deposition and the optimization of the sintering temperature to avoid the migration of Zr and Sr through the barrier layer as well as to limit the loss of Gd dopant can be found in the following reference [1]. After that, a cathode consisting of two layers, with thickness of ca. 15 μm each, including GDC and $(\text{La}_{0.6},\text{Sr}_{0.4})(\text{Co}_{0.2}\text{Fe}_{0.8})\text{O}_{3-\delta}$ (LSCF) in the first layer and LSCF in the second layer was screen printed on top of the barrier layer and sintered at 1100 $^\circ\text{C}$. Finally, a $(\text{La},\text{Sr})\text{CoO}_{3-\delta}$ layer was printed as electrical contact layer. The cell active area, corresponding to the cathode surface, was equal to 80 cm^2 .

Aging of the cells

Three cells of each type were placed in a stack made of 33 repeating units grouped in 11 clusters of cells with identical design and composition. Reference cells occupied the positions 6-7-8 and the cells with the PLD layer the positions 9-10-11. The stack was electrochemically tested in SOFC mode for 14000 h over a total of 17000 h (almost 2 years), including stops for maintenance. Ferritic stainless steel cassettes coated by ceramic protective coating to prevent Cr evaporation were used as interconnectors. The gas tightness between the anode and cathode chambers was ensured by a glass ceramic seal. Long-term operation was carried out by reproducing realistic operating conditions, which consisted in feeding the stack with desulfurized natural gas partially steam reformed at a current density of 0.4 $\text{A}\cdot\text{cm}^{-2}$, corresponding to 80 % of fuel utilization. Air was sent at the cathode. The gases were pre-heated before entering the stack and the operating temperature was self-sustained by the exothermic reaction. It was set to 760 $^\circ\text{C}$ for 10000 h (corresponding to 8000 h of real operation) and then lowered to 720 $^\circ\text{C}$ until the end of the test. More details about the test bench and this specific test are presented in previous works [1,30].

Post-mortem characterisation of the cells

Post-mortem analysis was performed on one operated cell of each type (with screen-printed barrier layer and with PLD barrier layer) as well as on one pristine screen-printed large-area

cell. The study of the barrier layers was performed by a complementary characterisation of the cell cross-section by Scanning Electron Microscopy (SEM), Electron Probe Micro Analysis with Wavelength Dispersive X-Ray Spectroscopy (EPMA-WDS), nano-XRF, Confocal Laser Raman Spectroscopy and TEM.

Cross-section microstructure was examined by a Zeiss Auriga SEM. The cells were simply fractured and embedded in an epoxy resin. Primary elemental analysis was performed with a JEOL JXA-8230 SEM equipped with an EPMA-WDS of 0.5 μm spatial resolution. This technique was selected instead of Energy Dispersive X-Ray spectroscopy (EDS) due to an overlap of the emission lines for the $L\alpha$ -series in the characteristic X-ray spectra of Sr and Zr that makes difficult the detection of SrZrO_3 . In order to determine the elemental distribution with nanometre resolution across the barrier layer, 1-2 μm thick and 20 μm long lamellas were prepared by FIB from the cross-section of embedded cell pieces in order to contain all the layers of interest. Those lamellas were then analysed by nano-XRF at the ID16B beamline of the European Synchrotron Radiation Facility (ESRF) [31]. The X-ray beam was focused down to $55 \times 48 \text{ nm}^2$ (VxH). Two multi-element Si-drift detectors (3 and 7 elements, 50 mm^2 of active area each) provided a high sensitivity for the detection of the XRF signals. The X-Ray energy of 29.5 keV was used to excite the $K_{\alpha,\beta}$ -XRF lines of the Zr, increasing the sensitivity to small changes in the distribution of this element that could not be detected in other studies where the L-lines of this element were detected [15,32]. The lamellas were scanned over an area of $8 \times 7 \mu\text{m}^2$ using a piezo-motor stage with a step size of $25 \times 25 \text{ nm}^2$ and accumulation times of 400 ms for both operated cells and 100 ms in the case of the pristine reference. The XRF data was fitted using the PyMca software in a pixel-by-pixel basis, and the fitting results enabled to plot intensity maps for each elemental XRF emission line over the studied area [33]. Raman spectra were recorded along the YSZ/CGO/LSCF cross section using a high resolution, confocal Spectrometer HR800 (LabRAM Series, Horiba Jobin Yvon). An excitation line of 532 nm and a 100x objective were employed. The laser spot size was equal to 0.5 μm . High Resolution TEM (HR-TEM), High Angle Annular Dark-Field (HAADF) STEM imaging, EDS mapping and Electron Energy Loss Spectroscopy (EELS) analysis of the lamellas were performed using a JEOL 2010F and a JEOL 2100 operated at 200 kV.

Results

1. Cells performance

Stacks including three reference cells with screen-printed BLs and three cells with PLD BLs were operated in SOFC mode for 14000 h over a total of 17000 h (almost 2 years). Figure 1a shows the temperature of the stack (measured at the air outlet) while the evolution with time of the average voltage for those six cells is presented in Figure 1b. First, from Figure 1a, one can observe that the stack suffered several stops during the two years of operation due to unexpected power cuts or required maintenance actions. In particular, the stop at ~ 2000 h was carried out to improve the thermal insulation of the system that resulted in an increase of the operation temperature (since the operation was self-sustained by the exothermic reactions occurring inside the stack). Initially, the cells with the PLD barrier layer presented 4% higher performance (voltage difference at constant current) than the reference ones (Figure 1b), showing that the barrier layer fabrication process has direct impact on the initial performance. In concrete terms, the PLD barrier layer induces a decrease of the cell serial resistance, as previously observed with button cells [1]. One can see that the performance enhancement with

large-area cells placed in a stack is less pronounced than with button cells, where an increase of 70% on the maximum power was obtained at 750 °C. However, the button cell is typically tested at very low fuel utilisation, therefore the contribution of the barrier layer dominates the electrochemical performance. On the other hand, the test on the stack is done at ca. 80% fuel utilization, where some contributions of concentration losses at the anode become significant with respect to the improvement due to the barrier layer. It is also important to consider that, at the stack level, a number of components are added that impact on the overall serial resistance, with a strong predominance of the losses related to the electrical contacts between electrodes and interconnects.

According to the operation temperature, three main operating periods can be defined: i) from the beginning to 2000 h, where the temperature was *ca.* 720 °C; ii) from 2650 h to 10200 h, where the temperature increased up to *ca.* 755 °C; and iii) from 10200 h to 17000 h, where the temperature was decreased to *ca.* 720 °C in order to highlight the difference in performances between the two types of cells. Both types of cells experienced a voltage drop in the first 550 h likely associated to the particle coarsening and to the stabilisation of the microstructure, as previously reported in the literature. The second operating period, corresponding to 5800 h of effective operating time, presented a lower degradation rate (even though the cells with PLD barrier layer suffered an increase of degradation during the last 1000 h of this period at higher temperature that resulted in the same voltage for both types of cells). After decreasing the temperature from ~ 755 °C to ~ 720 °C, the cells with PLD barrier layer recovered higher performance than the reference ones and showed higher stability. Overall, cells including PLD barrier layers maintained higher performance than the reference cells during most of the operating time.

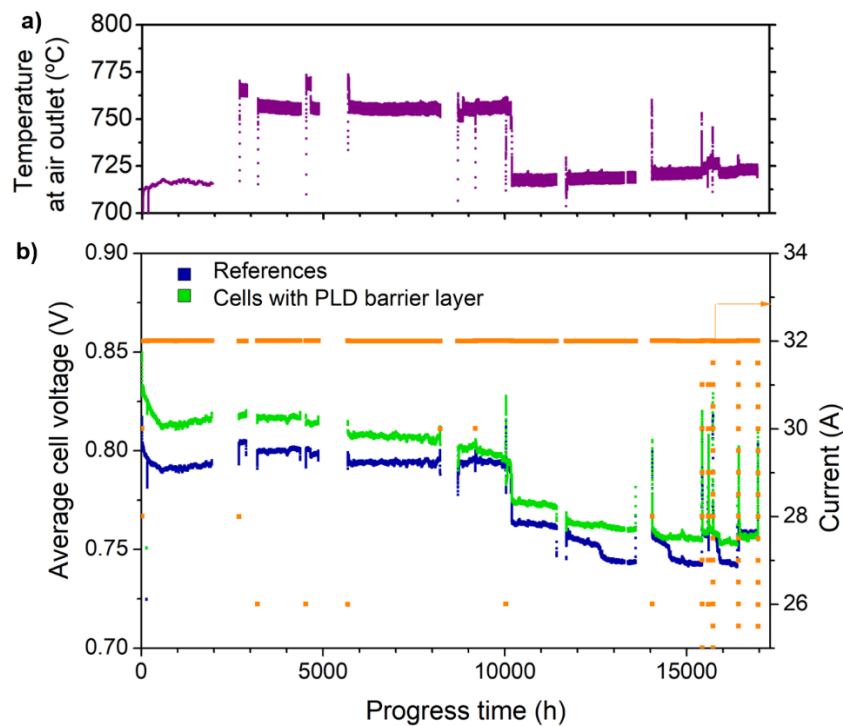


Figure 1. Evolution of a) the air outlet temperature and b) the average cell voltage from the three reference cells and from the three cells made with the PLD barrier layer over 14000 h of effective operating time.

2. Microstructural characterisation

Differences in the microstructures of operated reference cells made with screen-printed barrier layers and cells made with PLD barrier layers after operation can be observed in Figure 2. Cross-section SEM micrographs of conventional cells (Figure 2a-c) show the porous microstructure of screen-printed barrier layers, which is known to be a preferential location for SrZrO₃ formation [14]. According to these pictures, the barrier layer thickness is around 1.5 μm. In general, there is not delamination of the electrodes along the barrier layer interface. However, a horizontal crack inside the electrolyte is observed close to the barrier layer in several pieces of the cell (see Figure 2a). The fracture has been found in regions located near the fuel inlet, from where the gas flow arrives to the cell, or at fuel the outlet, where the gas leaves the cell. Figure 3 shows a closer view of the crack. This crack is parallel to the barrier layer but located inside the electrolyte (at ~ 2 μm from the interface between the barrier layer and the oxygen electrode). Moreover, the fracture seems to follow preferentially grain boundary shapes. The detail of the ends of the crack (Figure 3-b) indicates the presence of voids, which connect to each other when getting closer to fully fragmented part (Figure 3-c and d). Interestingly, the cells with the PLD barrier layer do not present any crack after careful SEM exploration. As seen in Figure 2d-f, a PLD barrier layer of ~ 1.5 μm in thickness is perfectly defined without showing any sign of oxygen electrode delamination or fracture formation. Only higher magnifications images show the presence of small voids inside the barrier layer (Figure 2-f). However, similar phenomena was already seen in as-fabricated PLD layers [22], so it cannot be necessarily attributed to the operation of the cell.

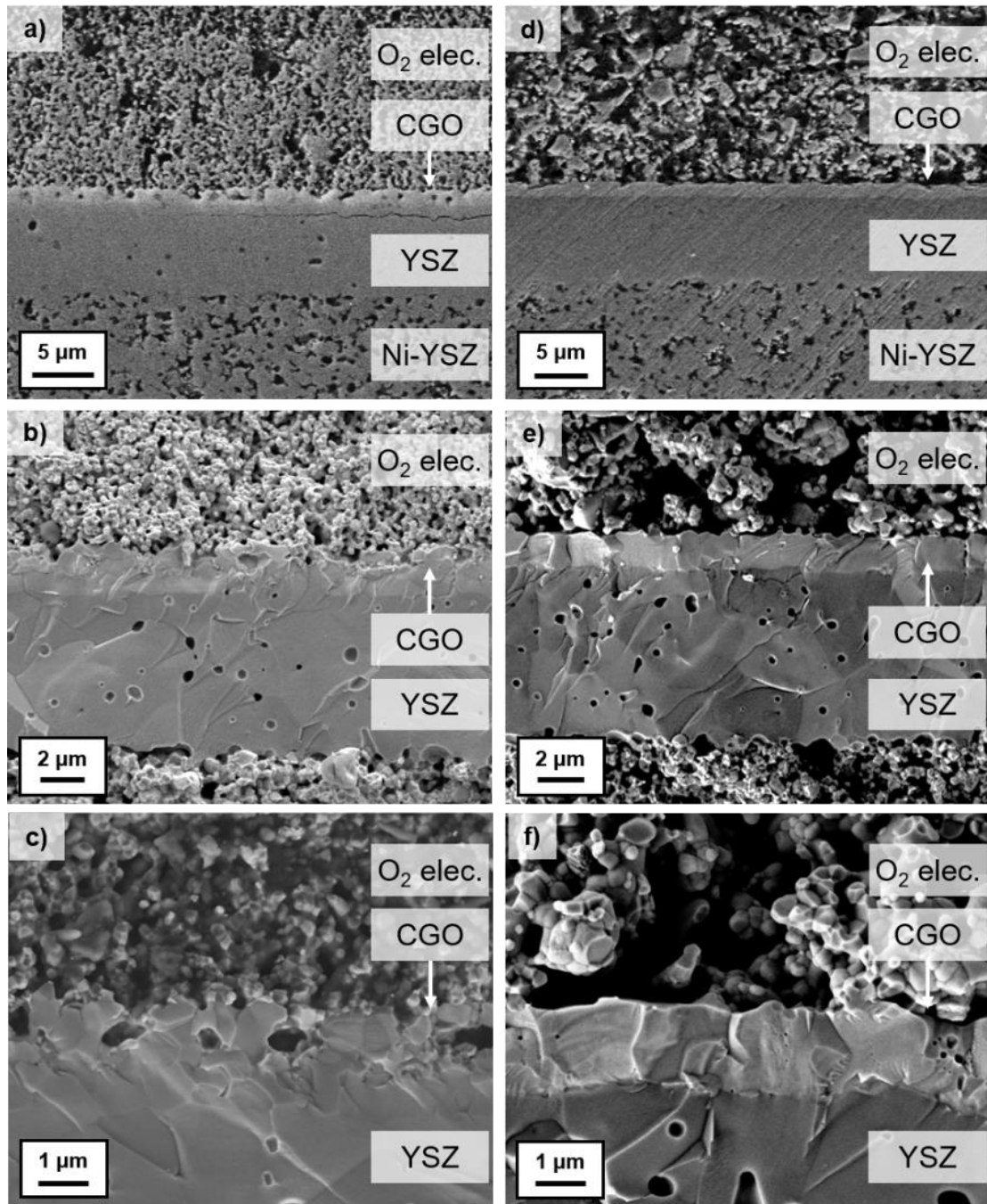


Figure 2. SEM images of the reference cell (a-c) and the cell with PLD barrier layer (d-f) both operated for 14000 h. Images a) and d) were obtained from polished cross-sections while images b), c) e) and f) were taken from fractured samples.

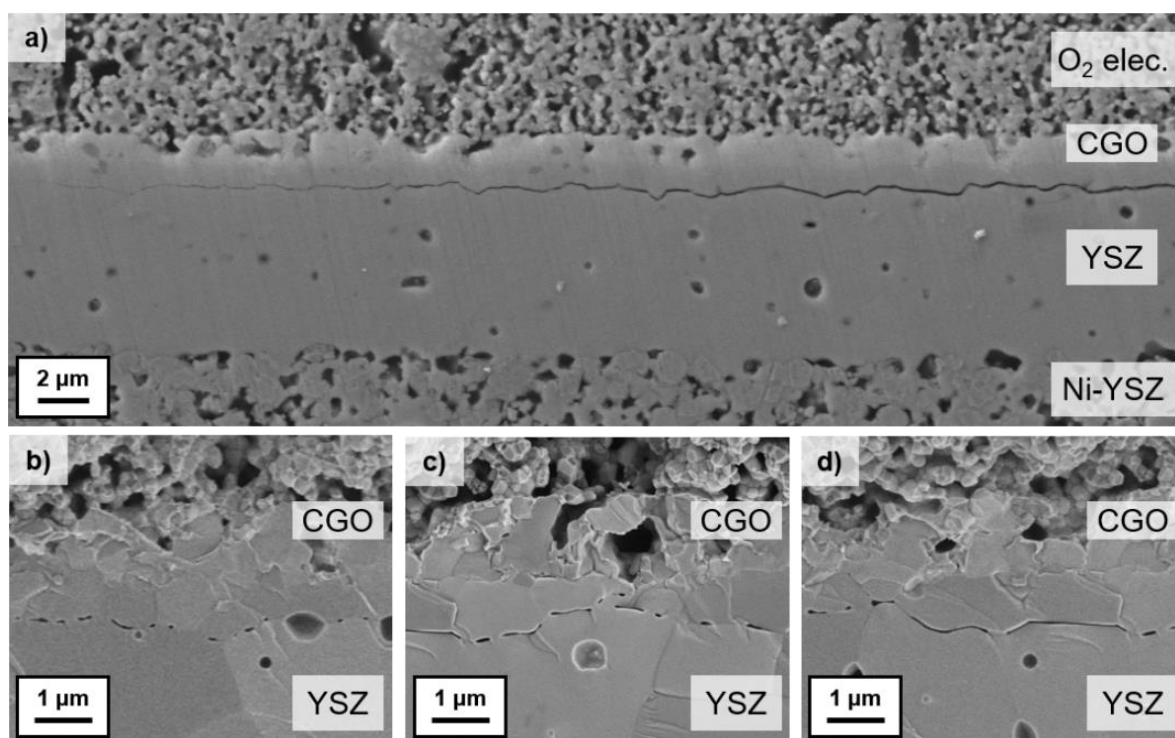


Figure 3. SEM images centred on the horizontal crack formed *inside* the electrolyte of the reference cell after 14000 h of effective operation. General view from a polished cross-section (a) and higher magnification of the end of the crack (b) and closer regions to the centre (c, d) from a fractured sample.

3. Chemical analysis

To better understand cationic interdiffusion across interfaces, elemental maps of the cross-section for the pristine reference cell, the operated reference cell (with screen-printed barrier layer) and operated cell made with the PLD barrier layer were measured by XRF with nanometric resolution. Figure 4 displays these elemental maps in logarithmic scale for Zr, Sr, Ce and Gd which correspond to the relevant atoms included in the LSCF-CGO oxygen electrode, the YSZ electrolyte and the CGO barrier layer. Dashed lines indicate the expected position of the interfaces between the different layers. Complementary elemental maps (La, Fe, Co and Y) in logarithmic scale are available in Figure S1, and maps in linear scale with line profiles of all the elements can be seen in Figures S2-4 of the Supplementary Information. The evolution of the La and Fe distribution is commented in detail in the Supplementary Information. Also, line profiles obtained by EPMA are reported in Figures S5.

Looking first at the pristine reference cell (Figure 4a, Figure S1a, Figure S2), one can observe some Zr and Sr overlapping regions within the barrier layer, but close to the electrolyte, which likely correspond to the well-known formation of SrZrO_3 during the sintering step of the LSCF electrode [14,15,32,34]. Beyond these small regions, one can see the presence of Zr and Y all over the CGO barrier layer ($\sim 1.5\text{-}2.0\ \mu\text{m}$) suggesting the formation of YSZ-CGO solid solution regions. Complementary, Ce and Gd strongly diffuse towards the electrolyte side forming a perfectly defined diffusion front at $0.6\ \mu\text{m}$. Finally, one can observe the presence of some Co where the Gd rich layer is located, as well as along the grain boundaries of the electrolyte, indicating fast rapid diffusion along the grain boundaries (Figure S1a).

After 14000 h of effective operation of the reference cell, one can observe a clear evolution of the composition of the different layers (see Figure 4b, Figure S1b and Figure S3). Special attention was paid to prepare the lamella of this cell in a region containing the crack present in the electrolyte (highlighted as a dashed white line in the figures). Regarding the overlapping between the diffusion of Zr and Sr within the barrier layer, there is no evidence of an increase in their concentration or extension. In this regard, no drastic changes in the amount or distribution of SrZrO_3 can be observed, meaning that this deleterious phase is mostly formed during the cell fabrication. Opposite, Zr and Y seem to strongly diffuse during the operation, homogeneously spreading inside the barrier layer and beyond, therefore reinforcing the idea of the formation of CGO-YSZ solid solution. Regarding the well-defined Ce/Gd diffusion fronts observed in the pristine cell inside the electrolyte, they penetrate longer distances for the operated cell (up to $\sim 0.8 \mu\text{m}$ for Gd) perfectly matching with the location of the fracture line. Additionally, Gd penetrates deeper into the electrolyte by diffusing through the grain boundaries. Finally, one can also observe strong migration of Fe and Co towards the electrolyte direction during the cell operation (Figure S1b). Several particles, principally containing Fe and Co, not present in pristine cells are observed after operation. In this regard, log scale maps of Co show a concentration increase of this element inside the electrolyte close to the crack (principally at the grain boundary level).

Opposite to the evolution showed by conventional cells, PLD cells after operation present very well defined interfaces and very small interdiffusion (Figure 4c, Figure S1c and Figure S4). First, overlapping of Sr and Zr is not observed within the barrier layer suggesting small or null formation of SrZrO_3 . Similarly, there is not interdiffusion of YSZ and CGO, which indicates that the potential solid solution formation (if any) will not have strong impact. Similarly, Figure S4b and Figure S5c reveal a very sharp transition from the electrolyte to the barrier layer, without any evidence of an enriched layer of Gd or diffusion front within the electrolyte (as observed for cells with screen-printed barrier layers). Finally, Co was not detected, even in logarithmic scale (Figure 4c), across the barrier layer or electrolyte.

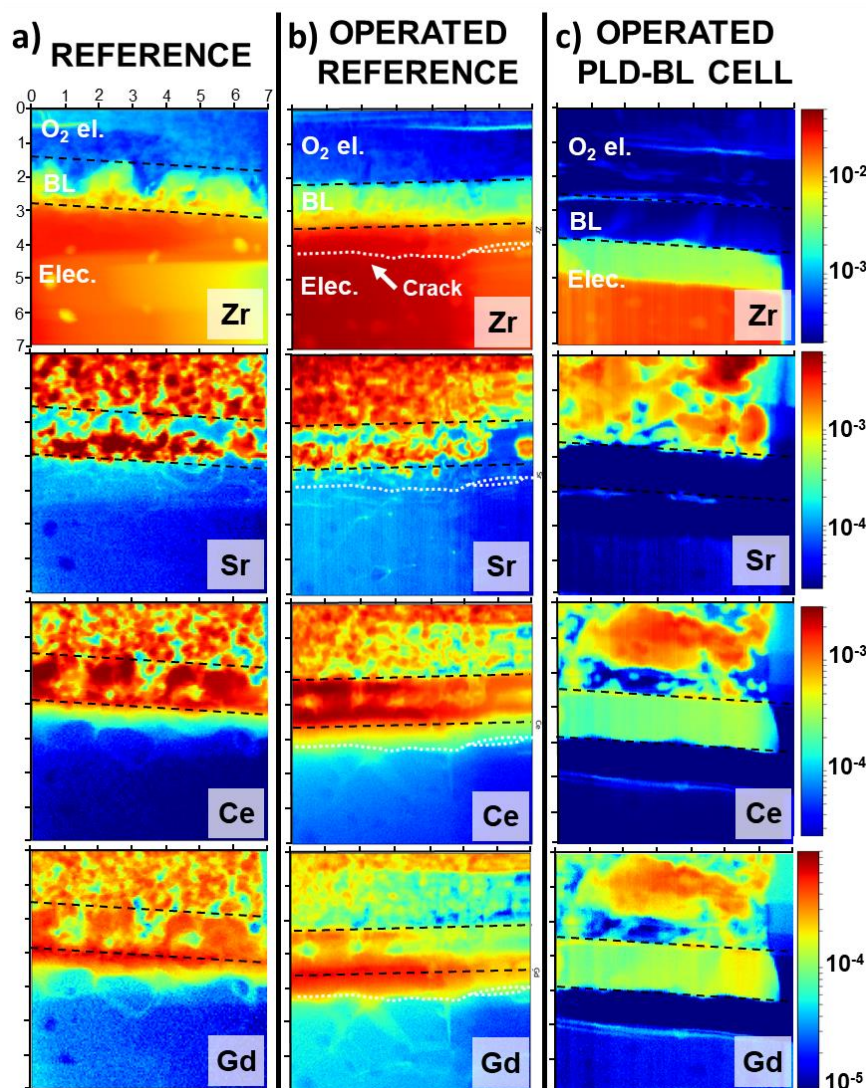


Figure 4. 2D element mappings in logarithmic scale obtained from the XRF signal for the a) pristine reference cell, b) the operated reference cell and c) for the operated cell with the PLD barrier layer. The x and y scales are in μm . The colour change within the electrolyte of the mappings from the operated PLD-BL cell (c) are coming from a change in thickness.

4. Structural analysis

4.1. Raman analysis

Figure 5 shows Raman spectra for each type of cell obtained every $0.5 \mu\text{m}$ along the cross-section of the cell. Here, measurements of the inlet part of the cells are presented (similar results are obtained for the outlet region as seen in Figure S6). Despite LSCF does not present Raman active modes, CGO and YSZ have very characteristic bands that depend on the dopant content or crystal structure [35,36].

Regarding the reference cell (Figure 5a), one can see that the most intense peak in the region of the cathode and the barrier layer corresponds to the F_{2g} mode of the CGO. It shifts from 450 cm^{-1} , inside the cathode, to 465 cm^{-1} , at the interface between the barrier layer and the electrolyte. The origin of this shift is compatible with a loss of Gd dopant [14,35]. When reaching the electrolyte, the same peak shifts until 469 cm^{-1} while broadening, which is likely related to the formation of a solid solution between CGO and YSZ (observed by Khun et al. at

470 cm^{-1} for $\text{Ce}_{0.95}\text{Zr}_{0.05}\text{O}_2$ [37]). Moreover, the presence of Raman signals from CGO and YSZ materials over an extended area of 1.5 – 2 μm indicates the coexistence of phases (main peaks at $\sim 465 \text{ cm}^{-1}$ for CGO and 620 cm^{-1} for tetragonal YSZ, observed from the light green line to the light red line). The YSZ Raman band around 620 cm^{-1} can be ascribed to the cubic or a particular tetragonal structure of zirconia ($t''\text{-ZrO}_2$), which is similar to stabilized cubic phase but with the presence of a high concentration of dislocations [38]. Despite cubic phases are typically expected for 8YSZ, $t''\text{-ZrO}_2$ phase was previously reported for doped zirconia with 8 to 9 mol.% Y_2O_3 [36]. Finally, a peak around 692 cm^{-1} was detected all across the electrolyte until the electrolyte-barrier layer interface possibly corresponding to the presence of Co_3O_4 [39].

Looking at the Raman spectra of the operated reference (Figure 5b) several changes are visible indicating an evolution of the local structure of the materials. First of all, the shift of the CGO main peak is more pronounced, changing from 450 cm^{-1} inside the cathode to 476 cm^{-1} at the interface barrier layer/electrolyte, which could correspond to higher proportion of Zr into the Ce/Zr (including Gd and Y) solid solution [37]. Furthermore, the coexistence of the YSZ and CGO phases is extended over a wider area, from the first micron of the cathode (light blue line) until the electrolyte (orange line). Interestingly, the YSZ peak at 249 cm^{-1} is shifted toward higher values (up to 270 cm^{-1}) inside the barrier layer, which is compatible with the occupation of tetragonal sites of YSZ by Ce^{4+} [40]. Finally, the Co_3O_4 peak at 692 cm^{-1} is more intense being present all around the operated cell (from 2 μm inside the cathode to the interface of the barrier layer and the electrolyte). The presence of two smaller peaks at 195 cm^{-1} and at 522 cm^{-1} , also corresponding to Co_3O_4 , are clearly visible in the samples where the main peak is revealed with a higher intensity [39].

Opposite to the reference cells, the PLD-barrier layer device presents a much simpler distribution of peaks easily assignable to simple phases (Figure 5c). For example, a much smaller shift of the main CGO Raman band is observed, which, combined with the negligible presence of YSZ within the barrier layer, indicates the great diffusion blocking capabilities of the PLD layer. In the same direction, a very small intensity of the main Co_3O_4 peak is observed in this cell at 695 cm^{-1} and restricted to a small region from the first 0.5 μm of the cathode (light blue line) to the electrolyte (light red line).

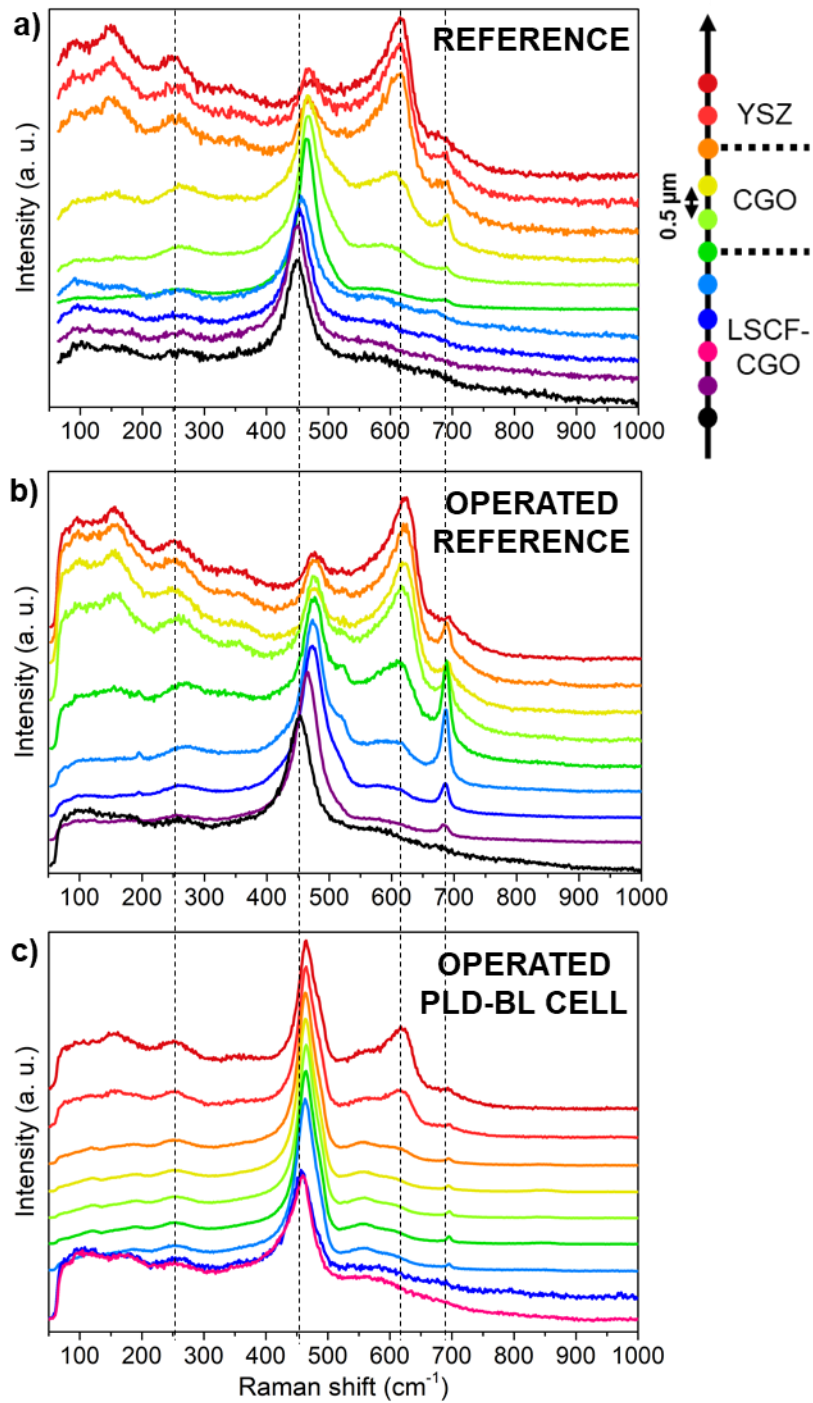


Figure 5. Raman microprobe spectra measured every $0.5 \mu\text{m}$ on a cell cross-section, at the interlayer YSZ/CGO/LSCF-CGO of a) the pristine reference cell, b) the operated reference cell and c) the operated cell made the PLD barrier layer.

4.2. TEM analysis

HR-TEM imaging, EELS/EDS mapping and Selected Area Electron Diffraction (SAED) were carried out for different regions of prepared cross-section lamellas of the different cells (the full study can be found in the TEM section of the supplementary information). EDS line scan profiles across the interface between the electrolyte and the CGO barrier layer, confirm that Ce, Gd, Zr and Y interdiffuse for more than 600 nm for the reference cell, while they diffuse

beyond 1.5 μm for the operated cell with the screen-printed barrier layer (see Figure 6a and Figure 6b, respectively). It is important to highlight that big amounts of Zr and Y were found in the barrier layer region. Moreover, some Co-Fe-rich particles were found located inside the screen-printed barrier layer for the pristine reference and deeper inside the interdiffusion zone in the case of the operated cell (see Figure S7). Opposite, for the cells fabricated with the PLD barrier layer, a very sharp interface without relevant interdiffusion (of only few nanometers) is observed even after operation for more than 14000 h (Figure 6c and EELS in Figure S8).

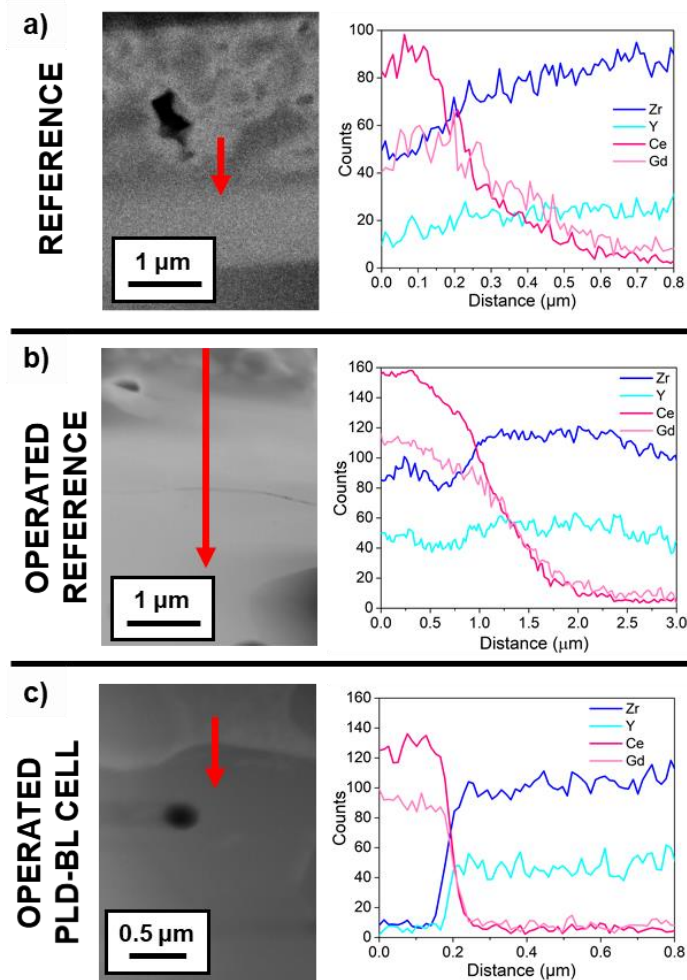


Figure 6. TEM image and EDS line scan profiles of a) the pristine reference cell, b) the operated reference cell and c) the operated cell made the PLD barrier layer.

TEM analysis was also employed to determine the nature of the observed fracture within the electrolyte. SAED of the operated reference cell reveals the presence of a tetragonal phase with different orientation in every of the sides of the fracture, indicating that the crack was propagated through a grain boundary (Figure 7a). Moreover, EELS analysis across the fracture undoubtedly shows that Ce (or Gd) did not diffuse beyond the crack (Figure 7b), at least using the bulk pathway. This result suggests that the crack was formed in the limit of Ce/Gd diffusion front (an alternative explanation suggesting that the formation of the crack stopped the diffusion of the cations within the electrolyte can be discarded since when the crack presents intragranular propagation the diffusion of cations is also stopped at the grain boundaries level, see Figure S9).

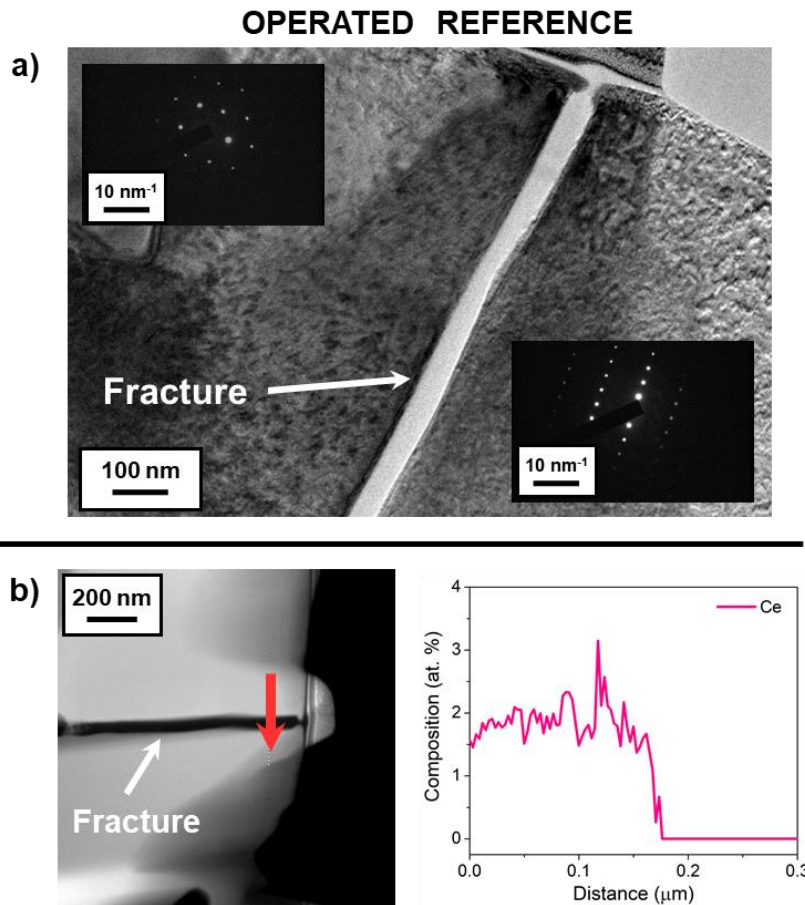


Figure 7. a) TEM image around the fracture visible in the operated reference cell with electron diffraction on both sides, showing two different grains. b) HAADF images and EELS spectrum profile of Ce across the fracture present in the operated reference cell.

Beyond the sharp interface previously mentioned for the cell with the PLD barrier layer, one can see in Figure 8 that the CGO barrier layers of both pristine and operated cells present a high density of dislocations and other crystallographic defects close to the interface with the electrolyte that are not present inside the YSZ. Moreover, Fast Fourier Transforms from the HR-TEM images obtained at the frontier CGO/YSZ of Figure S10 show that the CGO and YSZ crystals are almost perfectly aligned, meaning that the CGO barrier layer made by PLD is epitaxial. The nature of this interface could definitely contribute to have an excellent oxygen diffusivity from the electrolyte towards the barrier layer, improving the performance of the whole cell.

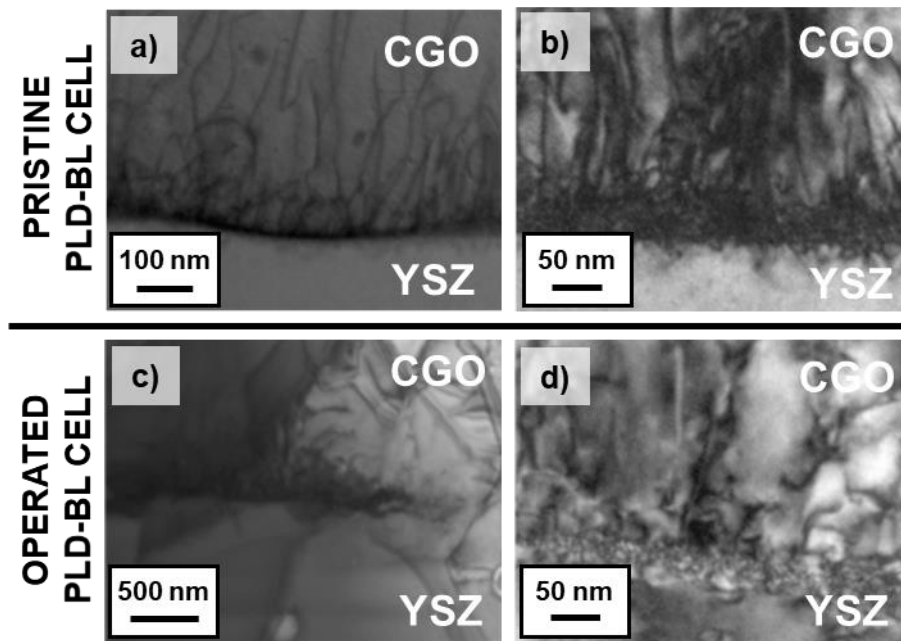


Figure 8. Bright Field image at the interface barrier layer/electrolyte of a) and b) a pristine cell made with the PLD barrier layer and c) and d) for the aged cell made with the PLD barrier layer.

Discussion

1. Degradation phenomena of the reference cell with screen-printed barrier layer

1.1. Formation of SrZrO_3

The presence of SrZrO_3 in the reference cell is clearly shown by the nano-XRF results (Figure 4 and Figure S2), EDS results (Figure S7) and the EPMA results (Figure S5a). The porous barrier layer presents high concentration of Sr and Zr, located at the same spots, in the pristine and the operated cell. The formation of SrZrO_3 during the manufacturing process of a cell made with a porous barrier layer sintered at high temperature is well known [9,41]. The barrier layer microstructure and its sintering temperature are two key parameters to limit the formation of SrZrO_3 [7]. Morales et al. explained that first of all the Zr and Y are diffusing through the grain boundaries and free surfaces of the CGO barrier layer during the high temperature sintering step of this layer, while Ce and Gd are diffusing into the electrolyte. During the cathode sintering, Sr from the cathode material diffuses mainly through the free surfaces and in less extent along the grain boundaries. Sr diffusion in gas-phase through volatile Sr-species is also considered as a possible way to transport Sr across the barrier layer pores, leading to the formation of SrZrO_3 where Zr is already present [14]. The presence of SrZrO_3 has a direct detrimental impact on the cell performance due to a reduction of the ionic conductivity of the barrier. On the other hand, the presence of this phase is also an indication of a decomposition of the LSCF cathode, and might act as Sr getter. The loss of Sr from the perovskite structure is known to produce a reduction of the ionic conductivity [42]. After operating the reference cell for 14000 h, the results presented in this work do not evidence a clear increase of SrZrO_3 inside the barrier layer. This is consistent with results reported in literature [14,15,43] even though SrZrO_3 formation during operation in SOFC has also been reported in some cases [23].

1.2. Crack formation inside the electrolyte: interdiffusion of YSZ and CGO

The results presented above clearly evidence the interdiffusion of Zr/Y from the electrolyte and Ce/Gd from the barrier layer. This phenomena, observed in the pristine reference cell, was expected as a consequence of the high sintering temperature (≥ 1300 °C) required for an appropriate densification [9]. XRF 2D-maps and line scans (Figure 4a, Figure S1a and Figure S2) show that this interdiffusion zone is extended over $1.7 \mu\text{m}$, which is also evidenced by EPMA (Fig S5a) and Raman spectra (Figure 5a). Zr and Y are penetrating the CGO barrier layer following mainly the same profile (see Figure S2b and Figure 6a). On the contrary, longer diffusion profiles are detected for Gd (than for Ce) inside the electrolyte. This phenomenon was reported for the first time by Uhlenbruck et al. [6] in 2009 but only gained attention in the past years [9,13–15,32]. It was found that Gd has a higher diffusion rate and solubility in YSZ than Ce and diffuses through the grain boundaries [6,14]. This is confirmed by the map presented in log scale in Figure 4. The formation of this Gd-enriched YSZ layer has a double impact on the cells' performance. On one side it probably results in a decrease of the barrier layer conductivity because of the loss of Gd from the doped ceria [44]. On the other side, one can expect a decrease of the YSZ layer that contains Gd. Indeed, results from literature show that the conductivity of a YSZ phase enriched with 5 mol% of Gd_2O_3 was found to be one order of magnitude lower than YSZ, reaching two orders of magnitude in the case of a 10 mol% enriched layer [9,11]. Even though it has been reported that the formation of this interlayer during the sintering step of the barrier layer can play a role to prevent the formation of SrZrO_3 during the cathode sintering step, it appears that it did not play that role in the present cells (see section 1.1 of the discussion related to the SrZrO_3 formation) [7,9,45]. Therefore, the presence of this interlayer is likely detrimental for the cell from its fabrication.

Continued operation under current also has an impact on the migration of Zr, Y, Ce and Gd. Raman spectra of the cells (Figure 5b) show the coexistence of the YSZ and CGO peaks over a wider range, corresponding to an extension of the YSZ signal until the cathode/barrier layer interface. Moreover, results from the XRF analysis allow observing an increase of Ce and Gd inside the electrolyte, especially in the case of Gd. Both ions are going deeper inside the electrolyte, and the accumulation of Gd is more important than for Ce compared to the initial stage (see Figure 4b and Figure S3b), as also reported elsewhere [13,15]. Regarding the effect of an increased migration of YSZ and CGO formal species, it would result in a reduction of ionic conductivity. Indeed, Matsui et al., in artificially produced replicas emulating the compositions naturally found along a pristine cell and an aged cell, demonstrated a decrease of the ionic conductivity by increasing either the amount of Gd of the Gd-rich YSZ layer or the amount of Zr inside the CGO layer [13].

Interestingly, the horizontal crack visible on Figure 3 present on the lamella used for the XRF analysis, is located at the limit between the 8YSZ and the interdiffusion layer. More precisely, as seen on Figure 3, it appears at ca. $2.3 \mu\text{m}$ from the oxygen electrode/barrier layer interface (corresponding to ca. $0.8 \mu\text{m}$ from the barrier layer/electrolyte interface). SEM analysis allowed observing the presence of tiny pores at the crack edges, following the grain boundaries. By getting closer to the crack, those pores are elongating until connecting each other and properly forming a crack (Figure 3b to d). Some images obtained on a fractured cross section,

where a plane displacement from both sides of the crack is observed, allowed to observe the grain surface covered by the small pores (see Figure S11) that are mainly growing along the surface. Composition analysis performed by XRF showed that the pores are located at the limit between the interdiffusion layer CGO-YSZ and the YSZ electrolyte (Figure 4b and **¡Error! No se encuentra el origen de la referencia.** S3a) while the TEM results evidence that the fracture takes place at the grain boundary (Figure 7 and Figure S9).

Such type of pore formation, close to the barrier layer/electrolyte interface, had been mainly reported for long-term operated cells in SOEC [46,47] but not in SOFC operation mode. Dong et al. claimed that those pores can be formed inside the electrolyte in SOEC mode when there is an ionic diffusion bottleneck, inducing an electronic bottleneck that results either in an oxygen pressure overshoot or undershoot and so, in the formation of bubbles or voids. The ionic bottleneck is most likely caused by grain boundaries, which are known, in the case of YSZ, to have oxide-ion conductivity 100 times lower of that of the bulk. Simulation showed that a grain boundary with a oxide-ion conductivity 10^4 times lower than the one of the bulk electrolyte was creating a sharp drop of oxygen pressure, setting the limit between oxidant and reducing atmosphere within the electrolyte at this particular location [48]. Depending on the oxygen potential, either voids are formed by the accumulation of oxygen vacancies coming from the reduction of some of the cations present at this grain boundary, or bubbles are appearing after the evaporation of lattice or interstitial O^{2-} [49]. When operating in SOFC, however, lower oxygen potential difference as well as lower electrical potential between the anode and the cathode is expected, which does not favour the apparition of voids or bubbles. Conversely, the void formation mechanism (and coalescence of voids resulting in fractures) observed in this paper is fully compatible with a common interdiffusion scenario. The interdiffusion of species with different diffusivity is a well-known condition for producing the so-called Kirkendall voids [50]. These type of voids are formed just behind the fastest diffusing element due to the accumulation of cation vacancies. Although it is difficult to quantify the interdiffusion of elements in this work, it seems clear that diffusion of Y and Zr on the porous barrier layer will be much higher due to the well-known fast mobility of the cations along surfaces. Opposite, Ce and Gd diffusion is taking place across the dense bulk electrolyte until it reaches the first grain boundary, which is a diffusion barrier for perpendicular crossing. This would be the reason for accumulation of Kirkendall voids when the Ce/Gd diffusion front reaches the first grain boundary of the YSZ electrolyte. Although not previously mentioned in the literature, it is interesting to underline that a similar crack formation inside the electrolyte (at a similar distance) has been reported for a ten-year operated SOFC [51]. There, the crack formation was associated to sample preparation issues, completely discarded in the present work. It is important to notice that previous works on Kirkendall-void formation in YSZ/CGO interfaces resulted in defects within the CGO layers, which is opposite to this work [52]. However, in this original publication, two dense layers were employed leading to a dominating bulk diffusivity of elements, which resulted in the formation of voids behind CGO due to the lower diffusivity of Gd in YSZ.

1.3. Destabilisation of La, Co and Fe from the LSCF-CGO cathode

This section will focus on the diffusion and/or precipitation of La, Co and Fe from the LSCF material. Reported results from nano-XRF, EPMA, Raman, and TEM analysis are all consistent with a LSCF destabilisation during fabrication and operation under cathodic polarization. The presence of La was detected homogeneously inside the barrier layer of the pristine reference, with a limited proportion reaching the electrolyte, whereas Fe was found to be present inside the barrier layer in smaller quantity, following the same profile as La (Figure S1a and Figure S2). On the contrary, Co was found to segregate into Co-rich particles inside the cathode and more pronouncedly inside the barrier layer up to the electrolyte (Figure 4a). Raman spectra allowed to identify peaks of Co_3O_4 in the barrier layer and electrolyte, giving an insight on the nature of those particles. Even though many papers from literature report a demixing of LSCF after fabrication, they mainly refer to the segregation of Sr to form SrZrO_3 [41]. Only few papers report the here presented destabilisation of the LSCF cathode and the diffusion of La, Fe and Co [9,28,32,43,53]. Szász et al. found that SrZrO_3 could be non-homogeneously doped with La, Fe and Gd while some particles of CoO and GdFeO_3 were formed inside the porous CGO barrier during manufacturing [9]. Moreover it is worth mentioning that the presence of La inside a CGO barrier layer was only observed by Villanova et al., using nano-XRF technique such as the ones carried out in this study [32].

It is also evident that the long-term operation of the LSCF-based electrode enhanced the LSCF destabilisation. La and Fe were both detected in larger amounts inside the barrier layer and the electrolyte, following different profiles one to another, compared to the pristine cell. Actually, looking at the maps from Figure S1b and Figure S3, Fe is located on the same spots as La but also where big particles of Co are detected. Those Co-rich particles drastically increased in size and are present from the electrode to the YSZ/CGO interdiffusion limit. The higher signal of the peaks related to Co_3O_4 and the range extension of their detection confirm the increase of Co demixing from LSCF. Moreover, the TEM results (Figure S7) have shown a core-shell type structure with a Co-rich core and a Fe-Co rich outer part. This could be due to a preferential precipitation of Co and Fe on top of the cobalt oxide particles. The increase of LSCF degradation under polarisation was reported by several authors but mainly in SOEC mode [4,28,32,43,51,54–56]. Menzler et al. found that the LSCF, present close to the barrier layer of a cell taken from a stack operated in SOFC for 10 years, was fragmented into different chemical equilibrium composition, and attributed this fact to Cr contamination [51]. Indeed, contamination with Cr and/or sulphur has been evidenced as a major source of cathode degradation [57]. However, none of those elements were detected in the cells analysed in this work. Thanks to operando XRD, Hardy et al. observed the formation of Co-rich and Fe-rich (Fe,Co) spinel under cathodic polarisation between 700 and 800 °C with either dry air or humid air [3]. The presence of Co-rich particles was found to be predominant in SOEC mode compared to SOFC by Laurencin et al., which is associated to the increase of SrZrO_3 formation in anodic polarisation. The particles were identified as cobalt-ferrite type compound and appeared to not be detrimental for the barrier layer performance, thanks to their good electrical conductivity and thermal compatibility with CGO [43,58]. However, this decomposition might result in a loss of electronic and ionic conductivity of the cathode material as well as a decrease in electro-catalytic activity of the electrode [59].

2. Effect of the PLD barrier layer on the cell degradation

In comparison with the reference cell made with screen-printed barrier layer, the region around the barrier layer made with PLD does not show any evidence of cation interdiffusion. The results presented here above confirm that the PLD layer was still perfectly playing its role after 14000 h. The sharp boundary between the CGO film and the YSZ electrolyte that was observed by SEM (Figure 2), was confirmed by the element analysis conducted by XRF (Figure 4, Figure S1c and Figure S4) and EPMA (Figure S5) but especially by TEM (Figure 6c and Figure S8) thanks to its higher precision. A sharp transition of few nanometres is present between the barrier layer and the electrolyte, showing that the optimized deposition and annealing process designed to fabricate the PLD barrier layer allows an effective protection against YSZ and CGO interdiffusion, which have been pointed as a source of several degradation phenomena during cell manufacturing and long-term operation. Indeed, the lower deposition temperature and annealing process as well as the limited sintering temperature of the cathode plays a fundamental role into the limitation of the species interdiffusion. Another essential parameter might come from the structure of the barrier layer. Despite being grown on top of a polycrystalline YSZ electrolyte, it seems that the CGO columnar grains are epitaxial respect to the YSZ grain they are in contact with. De Vero et al. have shown that epitaxial configuration was limiting the Sr and Zr diffusion across the CGO barrier layer, some planes orientation being more blocking than other. They still observe some SrZrO₃ formation due to the presence of dislocations that act as fast diffusion pathways [25]. A high number of dislocations was also observed in the PLD barrier layer of the present cells (pristine and aged), as seen in Figure 8, which can explain the migration of traces of Sr and Zr visible on the nano-XRF mapping in log scale (Figure 4). However, this limited phenomenon is probably due to the location of those dislocations, mainly at the YSZ interface and not across the whole barrier layer thickness. Consequently, there is no evidence of SrZrO₃ or other detrimental species formation after 14000 h of operation and the cathode's elements diffusion is efficiently avoided thanks to the high density of the layer as evidenced by the XRF profiles of Figure S4b-c. Finally, having an effective barrier layer guaranteed a protection against a crack formation inside the electrolyte, in opposition to the cell made with the screen-printed barrier layer.

The results of this work demonstrate that dense layers deposited with physical vapour deposition techniques can be more performant and durable. Beyond the preservation against SrZrO₃, a maintenance of the integrity in the region around the barrier layer contributes to reduce ancillary ageing phenomena, making the cell more resilient to long-term damages. Moreover, considering that the thorough post-mortem analysis does not show evidences of cathode element diffusion through the layer, a much thinner layer might also show an appropriate blocking behaviour. In this respect, Riegraf et al. showed that electrolyte-supported cells made with 0.5 µm EB-PVD dense barrier layer did not present SrZrO₃ formation after fabrication and after a durability test in SOFC of 840 h. However, barrier layers of 0.15 and 0.3 µm could not prevent the SrZrO₃ formation [22]. The reason for this limitation might come from the defects when approaching the electrolyte substrate. If they are present over the whole barrier layer they might act as fast diffusion paths for Sr and Zr. This aspect will be further investigated in future work.

Conclusions

Microstructural evolution of screen-printed and PLD-grown CGO barrier layers deposited on large-area SOFCs was evaluated after 14000 h of operation within the very same stack. Cells with PLD barrier layer presented better performance and stability, and a similar degradation rate than the screen-printed reference cells. Due to fabrication processes, pristine reference cells already showed strong cation interdiffusion resulting in the presence of deleterious SrZrO_3 inside the pores of the barrier layer, partial LSCF destabilisation at the cathode side and the formation of solid solution YSZ-CGO interlayers between the barrier layer and the electrolyte. After operation, cells with screen-printed layers did not present significant changes in the amount of SrZrO_3 phase, although a higher interdiffusion of Zr, Y, Ce and Gd was observed. Moreover, a fracture was observed at the Gd-diffusion front limit inside the electrolyte. This crack formation is unambiguously attributed to a void coalescence, which is likely related to the Kirkendall effect due to the faster diffusivity of Zr and Y at the surface of the CGO porous barrier layers. Such microstructural degradation could be responsible of instability of the cell performance and would probably result in a dramatic failure in the long term. Opposite, post-mortem analysis of large-area cells with PLD barrier layers clearly evidenced its excellent stability toward long-term operation. The formation of a conformal dense barrier layer perfectly blocked the cation interdiffusion between electrolyte and cathode avoiding the formation of secondary phases such as SrZrO_3 and the destabilisation of the cathode. Consequently, no fracture was observed, which means that the electrolyte integrity was fully preserved. PLD barrier layers are then proved to be an effective solution to limit degradation phenomena induced by the interdiffusion between the electrolyte and the cathode even in the long-term.

Acknowledgements

The authors thank the ESRF for the beamtime granted for this work and the staff of ID16B for their support. This project has received funding from the European Union's Horizon 2020 research and innovation program under grant agreement n° 874577 (NewSOC). LY acknowledges support from the MINECO (Spain) through the IJC2018-037698-I grant. MICIIN project PID2019-106165GB-C21 is also acknowledged.

References

- [1] M. Morales, A. Pesce, A. Slodczyk, M. Torrell, P. Piccardo, D. Montinaro, A. Tarancón, A. Morata, Enhanced Performance of Gadolinia-Doped Ceria Diffusion Barrier Layers Fabricated by Pulsed Laser Deposition for Large-Area Solid Oxide Fuel Cells, *ACS Appl. Energy Mater.* 1 (2018) 1955–1964. <https://doi.org/10.1021/acsaem.8b00039>.
- [2] S.J. Mcphail, S. Frangini, A. Abaza, A. Hagen, A. Léon, A. Brisse, D. Vladikova, F.R. Bianchi, B. Bosio, P. Piccardo, R. Spotorno, H. Uchida, Addressing planar solid oxide cell degradation mechanisms : A critical review of selected components, (2021) 1–37. <https://doi.org/10.1002/elsa.202100024>.
- [3] J.S. Hardy, C.A. Coyle, J.F. Bonnett, J.W. Templeton, N.L. Canfield, D.J. Edwards, S.M. Mahserejian, L. Ge, B.J. Ingram, J.W. Stevenson, Evaluation of cation migration in lanthanum strontium cobalt ferrite solid oxide fuel cell cathodes: Via in-operando X-ray diffraction, *J. Mater. Chem. A.* 6 (2018) 1787–1801. <https://doi.org/10.1039/c7ta06856e>.
- [4] Y. Sun, S. He, M. Saunders, K. Chen, Z. Shao, S.P. Jiang, A comparative study of surface segregation and interface of $\text{La}_{0.6}\text{Sr}_{0.4}\text{Co}_{0.2}\text{Fe}_{0.8}\text{O}_{3-\delta}$ electrode on GDC and YSZ electrolytes of solid oxide fuel cells, *Int. J. Hydrogen Energy.* 46 (2021) 2606–2616. <https://doi.org/10.1016/j.ijhydene.2020.10.113>.
- [5] J. Laurencin, M. Hubert, D.F. Sanchez, S. Pylypko, M. Morales, A. Morata, B. Morel, D. Montinaro, F. Lefebvre-Joud, E. Siebert, Degradation mechanism of $\text{La}_{0.6}\text{Sr}_{0.4}\text{Co}_{0.2}\text{Fe}_{0.8}\text{O}_{3-\delta}/\text{Gd}_{0.1}\text{Ce}_{0.9}\text{O}_{2-\delta}$ composite electrode operated under solid oxide electrolysis and fuel cell conditions, *Electrochim. Acta.* 241 (2017) 459–476. <https://doi.org/10.1016/j.electacta.2017.05.011>.
- [6] S. Uhlenbruck, T. Moskalewicz, N. Jordan, H.J. Penkalla, H.P. Buchkremer, Element interdiffusion at electrolyte-cathode interfaces in ceramic high-temperature fuel cells, *Solid State Ionics.* 180 (2009) 418–423. <https://doi.org/10.1016/j.ssi.2009.01.014>.
- [7] V. Wilde, H. Störmer, J. Szász, F. Wankmüller, E. Ivers-Tiffée, D. Gerthsen, $\text{Gd}_{0.2}\text{Ce}_{0.8}\text{O}_2$ Diffusion Barrier Layer between $(\text{La}_{0.58}\text{Sr}_{0.4})(\text{Co}_{0.2}\text{Fe}_{0.8})\text{O}_{3-\delta}$ Cathode and $\text{Y}_{0.16}\text{Zr}_{0.84}\text{O}_2$ Electrolyte for Solid Oxide Fuel Cells: Effect of Barrier Layer Sintering Temperature on Microstructure, *ACS Appl. Energy Mater.* 1 (2018) 6790–6800. <https://doi.org/10.1021/acsaem.8b00847>.
- [8] R. Knibbe, J. Hjelm, M. Menon, N. Pryds, M. Søgaaard, H.J. Wang, K. Neufeld, Cathode-electrolyte interfaces with CGO barrier layers in SOFC, *J. Am. Ceram. Soc.* 93 (2010) 2877–2883. <https://doi.org/10.1111/j.1551-2916.2010.03763.x>.
- [9] J. Szász, F. Wankmüller, V. Wilde, H. Störmer, D. Gerthsen, N.H. Menzler, E. Ivers-Tiffée, Nature and Functionality of $\text{La}_{0.58}\text{Sr}_{0.4}\text{Co}_{0.2}\text{Fe}_{0.8}\text{O}_{3-\delta}/\text{Gd}_{0.2}\text{Ce}_{0.8}\text{O}_{2-\delta}/\text{Y}_{0.16}\text{Zr}_{0.84}\text{O}_{2-\delta}$ Interfaces in SOFCs, *J. Electrochem. Soc.* 165 (2018) F898–F906. <https://doi.org/10.1149/2.0031811jes>.
- [10] A. Tsoga, A. Gupta, A. Naoumidis, D. Skarmoutsos, P. Nikolopoulos, Performance of a double-layer CGO/YSZ electrolyte for solid oxide fuel cells, *Ionics (Kiel).* 4 (1998) 234–240. <https://doi.org/10.1007/BF02375951>.
- [11] T. Matsui, S. Li, H. Muroyama, K. Kishida, H. Inui, K. Eguchi, Electrochemical property of solid solutions formed in $(\text{La},\text{Sr})(\text{Co},\text{Fe})\text{O}_{3-\delta}$ cathode/doped- CeO_2 interlayer/ $\text{Y}_2\text{O}_3\text{-ZrO}_2$ electrolyte system during operation of solid oxide fuel cells, *Solid State Ionics.* 300 (2017) 135–139. <https://doi.org/10.1016/j.ssi.2016.12.014>.
- [12] H. Xu, K. Cheng, M. Chen, L. Zhang, K. Brodersen, Y. Du, Interdiffusion between gadolinia doped ceria and yttria stabilized zirconia in solid oxide fuel cells: Experimental investigation and kinetic modeling, *J. Power Sources.* 441 (2019)

227152. <https://doi.org/10.1016/j.jpowsour.2019.227152>.
- [13] T. Matsui, S. Li, Y. Inoue, N. Yoshida, H. Muroyama, K. Eguchi, Degradation Analysis of Solid Oxide Fuel Cells with (La,Sr)(Co,Fe)O_{3-δ} Cathode/Gd₂O₃ – CeO₂ Interlayer/Y₂O₃–ZrO₂ Electrolyte System: The Influences of Microstructural Change and Solid Solution Formation, *J. Electrochem. Soc.* 166 (2019) F295–F300. <https://doi.org/10.1149/2.0841904jes>.
- [14] M. Morales, V. Miguel-Pérez, A. Tarancón, A. Slodczyk, M. Torrell, B. Ballesteros, J.P. Ouweltjes, J.M. Bassat, D. Montinaro, A. Morata, Multi-scale analysis of the diffusion barrier layer of gadolinia-doped ceria in a solid oxide fuel cell operated in a stack for 3000 h, *J. Power Sources.* 344 (2017) 141–151. <https://doi.org/10.1016/j.jpowsour.2017.01.109>.
- [15] F. Monaco, D. Ferreira-Sanchez, M. Hubert, B. Morel, D. Montinaro, D. Grolimund, J. Laurencin, Oxygen electrode degradation in solid oxide cells operating in electrolysis and fuel cell modes: LSCF destabilization and interdiffusion at the electrode/electrolyte interface, *Int. J. Hydrogen Energy.* (2021). <https://doi.org/10.1016/j.ijhydene.2021.07.054>.
- [16] C. Nicollet, J. Waxin, T. Dupeyron, A. Flura, J.-M. Heintz, J.P. Ouweltjes, P. Piccardo, A. Rougier, J.-C. Grenier, J.-M. Bassat, Gadolinium doped ceria interlayers for Solid Oxide Fuel Cells cathodes: Enhanced reactivity with sintering aids (Li, Cu, Zn), and improved densification by infiltration, *J. Power Sources.* 372 (2017) 157–165. <https://doi.org/10.1016/j.jpowsour.2017.10.064>.
- [17] S. Molin, J. Karczewski, B. Kamecki, A. Mroziński, S.F. Wang, P. Jasiński, Processing of Ce_{0.8}Gd_{0.2}O_{2-δ} barrier layers for solid oxide cells: The effect of preparation method and thickness on the interdiffusion and electrochemical performance, *J. Eur. Ceram. Soc.* 40 (2020) 5626–5633. <https://doi.org/10.1016/j.jeurceramsoc.2020.06.006>.
- [18] S. Hwang, J. Lee, G. Kang, M. Choi, S.J. Kim, W. Lee, D. Byun, A hydrogel-assisted GDC chemical diffusion barrier for durable solid oxide fuel cells, *J. Mater. Chem. A.* 9 (2021) 11683–11690. <https://doi.org/10.1039/d1ta00507c>.
- [19] S. Sønderby, T. Klemensø, B.H. Christensen, K.P. Almtoft, J. Lu, L.P. Nielsen, P. Eklund, Magnetron sputtered gadolinia-doped ceria diffusion barriers for metal-supported solid oxide fuel cells, *J. Power Sources.* 267 (2014) 452–458. <https://doi.org/10.1016/j.jpowsour.2014.05.101>.
- [20] N. Coppola, P. Polverino, G. Carapella, C. Sacco, A. Galdi, A. Ubaldini, V. Vaiano, D. Montinaro, L. Maritato, C. Pianese, Structural and electrical characterization of sputter-deposited Gd_{0.1}Ce_{0.9}O_{2-δ} thin buffer layers at the Y-stabilized zirconia electrolyte interface for IT-solid oxide cells, *Catalysts.* 8 (2018). <https://doi.org/10.3390/catal8120571>.
- [21] N. Coppola, P. Polverino, G. Carapella, C. Sacco, A. Galdi, D. Montinaro, L. Maritato, C. Pianese, Optimization of the electrical performances in Solid Oxide Fuel Cells with room temperature sputter deposited Gd_{0.1}ce_{0.9}o_{1.95} buffer layers by controlling their granularity via the in-air annealing step, *Int. J. Hydrogen Energy.* 45 (2020) 12997–13008. <https://doi.org/10.1016/j.ijhydene.2020.02.187>.
- [22] M. Riegraf, F. Han, N. Sata, R. Costa, Intercalation of Thin-Film Gd-Doped Ceria Barrier Layers in Electrolyte-Supported Solid Oxide Cells: Physicochemical Aspects, *ACS Appl. Mater. Interfaces.* (2021). <https://doi.org/10.1021/acsami.1c11175>.
- [23] F. Wang, M.E. Brito, K. Yamaji, D.H. Cho, M. Nishi, H. Kishimoto, T. Horita, H. Yokokawa, Effect of polarization on Sr and Zr diffusion behavior in LSCF/GDC/YSZ system, *Solid State Ionics.* 262 (2014) 454–459. <https://doi.org/10.1016/j.ssi.2014.04.002>.

- [24] Z. Lu, S. Darvish, J. Hardy, J. Templeton, J. Stevenson, Y. Zhong, SrZrO₃ Formation at the Interlayer/Electrolyte Interface during (La_{1-x}Sr_x)_{1-δ}Co_{1-y}Fe_yO₃ Cathode Sintering, *J. Electrochem. Soc.* 164 (2017) F3097–F3103. <https://doi.org/10.1149/2.0141710jes>.
- [25] J.C. De Vero, K. Develos-Bagarinao, H. Matsuda, H. Kishimoto, T. Ishiyama, K. Yamaji, T. Horita, H. Yokokawa, Sr and Zr transport in PLD-grown Gd-doped ceria interlayers, *Solid State Ionics*. 314 (2018) 165–171. <https://doi.org/10.1016/j.ssi.2017.10.023>.
- [26] K. Develos-Bagarinao, R.A. Budiman, S.S. Liu, T. Ishiyama, H. Kishimoto, K. Yamaji, Evolution of cathode-interlayer interfaces and its effect on long-term degradation, *J. Power Sources*. 453 (2020) 227894. <https://doi.org/10.1016/j.jpowsour.2020.227894>.
- [27] G. Nurk, M. Vestli, P. Möller, R. Jaaniso, M. Kodu, H. Mändar, T. Romann, R. Kanarbik, E. Lust, Mobility of Sr in Gadolinia Doped Ceria Barrier Layers Prepared Using Spray Pyrolysis, Pulsed Laser Deposition and Magnetron Sputtering Methods, *J. Electrochem. Soc.* 163 (2016) F88–F96. <https://doi.org/10.1149/2.0531602jes>.
- [28] J.C. De Vero, K. Develos-Bagarinao, T. Ishiyama, H. Kishimoto, K. Yamaji, T. Horita, H. Yokokawa, Elucidating the Degradation Mechanism at the Cathode-Interlayer Interfaces of Solid Oxide Fuel Cells, *J. Electrochem. Soc.* 165 (2018) F1340–F1348. <https://doi.org/10.1149/2.0941816jes>.
- [29] M. Riegraf, I. Bombarda, F. Dömling, T. Liensdorf, C. Sitzmann, N. Langhof, S. Schafföner, F. Han, N. Sata, C. Geipel, C. Walter, R. Costa, Enhancing the Mechanical Strength of Electrolyte-Supported Solid Oxide Cells with Thin and Dense Doped-Ceria Interlayers, *ACS Appl. Mater. Interfaces*. (2021). <https://doi.org/10.1021/acsmi.1c13899>.
- [30] F. Alenazey, Y. Alyousef, E. Brancaccio, D. Montinaro, Parameters affecting CO₂ production in a planar anode supported SOFC based system, *Int. J. Hydrogen Energy*. 40 (2015) 642–651. <https://doi.org/10.1016/j.ijhydene.2014.10.110>.
- [31] G. Martinez-Criado, J. Villanova, R. Tucoulou, D. Salomon, J.P. Suuronen, S. Laboure, C. Guilloud, V. Valls, R. Barrett, E. Gagliardini, Y. Dabin, R. Baker, S. Bohic, C. Cohen, J. Morse, ID16B: A hard X-ray nanoprobe beamline at the ESRF for nano-analysis, *J. Synchrotron Radiat.* 23 (2016) 344–352. <https://doi.org/10.1107/S1600577515019839>.
- [32] J. Villanova, S. Schlabach, A. Brisse, A. Léon, X-ray fluorescence nano-imaging of long-term operated solid oxide electrolysis cells, *J. Power Sources*. 421 (2019) 100–108. <https://doi.org/10.1016/j.jpowsour.2019.02.084>.
- [33] V.A. Solé, E. Papillon, M. Cotte, P. Walter, J. Susini, A multiplatform code for the analysis of energy-dispersive X-ray fluorescence spectra, *Spectrochim. Acta Part B At. Spectrosc.* 62 (2007) 63–68. <https://doi.org/10.1016/J.SAB.2006.12.002>.
- [34] D.F. Sanchez, D. Grolimund, M. Hubert, P. Bleuet, J. Laurencin, A 2D and 3D X-ray M-diffraction and M-fluorescence study of a mixed ionic electronic conductor, *Int. J. Hydrogen Energy*. 42 (2017) 1203–1211. <https://doi.org/10.1016/j.ijhydene.2016.11.094>.
- [35] N. Yang, Y. Shi, S. Schweiger, E. Strelcov, A. Belianinov, V. Foglietti, P. Orgiani, G. Balestrino, S. V. Kalinin, J.L.M. Rupp, C. Aruta, Role of Associated Defects in Oxygen Ion Conduction and Surface Exchange Reaction for Epitaxial Samaria-Doped Ceria Thin Films as Catalytic Coatings, *ACS Appl. Mater. Interfaces*. 8 (2016) 14613–14621. <https://doi.org/10.1021/acsmi.6b03909>.
- [36] Y. Hemberger, N. Wichtner, C. Berthold, K.G. Nickel, Quantification of yttria in stabilized zirconia by Raman spectroscopy, *Int. J. Appl. Ceram. Technol.* 13 (2016)

- 116–124. <https://doi.org/10.1111/ijac.12434>.
- [37] M. Kuhn, S.R. Bishop, J.L.M. Rupp, H.L. Tuller, Structural characterization and oxygen nonstoichiometry of ceria-zirconia ($\text{Ce}_{1-x}\text{Zr}_x\text{O}_{2-\delta}$) solid solutions, *Acta Mater.* 61 (2013) 4277–4288. <https://doi.org/10.1016/j.actamat.2013.04.001>.
- [38] M. Yashima, K. Ohtake, M. Kakihana, H. Arashi, M. Yoshimura, Determination of tetragonal-cubic phase boundary of BY Raman scattering, *J. Phys. Chem. Solids.* 57 (1996) 17–24. [https://doi.org/10.1016/0022-3697\(95\)00085-2](https://doi.org/10.1016/0022-3697(95)00085-2).
- [39] I. Lorite, J.J. Romero, J.F. Fernández, Effects of the agglomeration state on the Raman properties of Co_3O_4 nanoparticles, *J. Raman Spectrosc.* 43 (2012) 1443–1448. <https://doi.org/10.1002/jrs.4098>.
- [40] D.-J. Kim, H.-J. Jung, I.-S. Yang, Raman Spectroscopy of Tetragonal Zirconia Solid Solutions, *J. Am. Ceram. Soc.* 76 (1993) 2106–2108. <https://doi.org/10.1111/j.1151-2916.1993.tb08341.x>.
- [41] M.Z. Khan, R.H. Song, M.T. Mehran, S.B. Lee, T.H. Lim, Controlling cation migration and inter-diffusion across cathode/interlayer/electrolyte interfaces of solid oxide fuel cells: A review, *Ceram. Int.* 47 (2021) 5839–5869. <https://doi.org/10.1016/j.ceramint.2020.11.002>.
- [42] E. Effori, J. Laurencin, E.D.R. Silva, M. Hubert, T. David, M. Petitjean, G. Geneste, L. Dessemond, E. Siebert, An Elementary Kinetic Model for the LSCF and LSCF-CGO Electrodes of Solid Oxide Cells: Impact of Operating Conditions and Degradation on the Electrode Response, *J. Electrochem. Soc.* 168 (2021) 044520. <https://doi.org/10.1149/1945-7111/abf40a>.
- [43] J. Laurencin, M. Hubert, D.F. Sanchez, S. Pylypko, M. Morales, A. Morata, B. Morel, D. Montinaro, F. Lefebvre-Joud, E. Siebert, Degradation mechanism of $\text{La}_{0.6}\text{Sr}_{0.4}\text{Co}_{0.2}\text{Fe}_{0.8}\text{O}_{3-\delta}/\text{Gd}_{0.1}\text{Ce}_{0.9}\text{O}_{2-\delta}$ composite electrode operated under solid oxide electrolysis and fuel cell conditions, *Electrochim. Acta.* 241 (2017) 459–476. <https://doi.org/10.1016/j.electacta.2017.05.011>.
- [44] B.C.H. Steele, Appraisal of $\text{Ce}_{1-y}\text{Gd}_y\text{O}_{2-y/2}$ electrolytes for IT-SOFC operation at 500 °C, *Solid State Ionics.* 129 (2000) 95–110. [https://doi.org/10.1016/S0167-2738\(99\)00319-7](https://doi.org/10.1016/S0167-2738(99)00319-7).
- [45] F. Wankmüller, J. Szász, J. Joos, V. Wilde, H. Störmer, D. Gerthsen, E. Ivers-Tiffée, Correlative tomography at the cathode/electrolyte interfaces of solid oxide fuel cells, *J. Power Sources.* 360 (2017) 399–408. <https://doi.org/10.1016/j.jpowsour.2017.06.008>.
- [46] F. Tietz, D. Sebold, A. Brisse, J. Schefold, Degradation phenomena in a solid oxide electrolysis cell after 9000 h of operation, *J. Power Sources.* 223 (2013) 129–135. <https://doi.org/https://doi.org/10.1016/j.jpowsour.2012.09.061>.
- [47] G. Rinaldi, S. Diethelm, E. Oveisi, P. Burdet, J. Van herle, D. Montinaro, Q. Fu, A. Brisse, Post-test Analysis on a Solid Oxide Cell Stack Operated for 10,700 Hours in Steam Electrolysis Mode, *Fuel Cells.* 17 (2017) 541–549. <https://doi.org/10.1002/fuce.201600194>.
- [48] Y. Dong, Z. Zhang, A. Alvarez, I.W. Chen, Potential jumps at transport bottlenecks cause instability of nominally ionic solid electrolytes in electrochemical cells, *Acta Mater.* 199 (2020) 264–277. <https://doi.org/10.1016/j.actamat.2020.08.017>.
- [49] Y. Dong, I.W. Chen, Electrical and hydrogen reduction enhances kinetics in doped zirconia and ceria: II. Mapping electrode polarization and vacancy condensation in YSZ, *J. Am. Ceram. Soc.* 101 (2018) 1058–1073. <https://doi.org/10.1111/jace.15274>.
- [50] H. Mitsuyasu, Y. Nonaka, K. Eguchi, Analysis of solid state reaction at the interface of yttria-doped ceria/yttria-stabilized zirconia, *Solid State Ionics.* 113–115 (1998) 279–284. [https://doi.org/10.1016/s0167-2738\(98\)00293-8](https://doi.org/10.1016/s0167-2738(98)00293-8).
- [51] N.H. Menzler, D. Sebold, Y.J. Sohn, S. Zischke, Post-test characterization of a solid

- oxide fuel cell after more than 10 years of stack testing, *J. Power Sources*. 478 (2020) 228770. <https://doi.org/10.1016/j.jpowsour.2020.228770>.
- [52] V.M. Bekale, A.M. Huntz, C. Legros, G. Sattonnay, F. Jomard, Impurity diffusion of cerium and gadolinium in single- and polycrystalline yttria-stabilized zirconia, *Philos. Mag.* 88 (2008) 1–19. <https://doi.org/10.1080/14786430701708331>.
- [53] J. Railsback, S.H. Choi, S.A. Barnett, Effectiveness of dense Gd-doped ceria barrier layers for (La,Sr)(Co,Fe)O₃ cathodes on Yttria-stabilized zirconia electrolytes, *Solid State Ionics*. 335 (2019) 74–81. <https://doi.org/10.1016/j.ssi.2019.02.020>.
- [54] C.E. Frey, Q. Fang, D. Sebold, L. Blum, N.H. Menzler, A Detailed Post Mortem Analysis of Solid Oxide Electrolyzer Cells after Long-Term Stack Operation, *J. Electrochem. Soc.* 165 (2018) F357–F364. <https://doi.org/10.1149/2.0961805jes>.
- [55] A. Mahmoud, M. Al Daroukh, M. Lipinska-Chwalek, M. Luysberg, F. Tietz, R.P. Hermann, A Mössbauer spectral study of degradation in La_{0.58}Sr_{0.4}Fe_{0.5}Co_{0.5}O_{3-x} after long-term operation in solid oxide electrolysis cells, *Solid State Ionics*. 312 (2017) 38–43. <https://doi.org/10.1016/j.ssi.2017.10.003>.
- [56] Z. Lyu, S. Liu, Y. Wang, H. Li, Z. Liu, Z. Sun, K. Sun, S. Zhang, M. Han, Quantifying the performance evolution of solid oxide fuel cells during initial aging process, *J. Power Sources*. 510 (2021) 230432. <https://doi.org/10.1016/j.jpowsour.2021.230432>.
- [57] H. Yokokawa, M. Suzuki, M. Yoda, T. Suto, K. Tomida, K. Hiwatashi, M. Shimazu, A. Kawakami, H. Sumi, M. Ohmori, T. Ryu, N. Mori, M. Iha, S. Yatsuzuka, K. Yamaji, H. Kishimoto, K. Develos-Bagarinao, T. Shimonosono, K. Sasaki, S. Taniguchi, T. Kawada, M. Muramatsu, K. Terada, K. Eguchi, T. Matsui, H. Iwai, M. Kishimoto, N. Shikazono, Y. Mugikura, T. Yamamoto, M. Yoshikawa, K. Yasumoto, K. Asano, Y. Matsuzaki, K. Sato, T. Somekawa, Achievements of NEDO Durability Projects on SOFC Stacks in the Light of Physicochemical Mechanisms, *Fuel Cells*. (2019) fuce.201800187. <https://doi.org/10.1002/fuce.201800187>.
- [58] L. Qiu, T. Ichikawa, A. Hirano, N. Imanishi, Y. Takeda, Ln_{1-x}Sr_xCo_{1-y}FeyO_{3-δ} (Ln=Pr, Nd, Gd; X=0.2, 0.3) for the electrodes of solid oxide fuel cells, *Solid State Ionics*. 158 (2003) 55–65. [https://doi.org/10.1016/S0167-2738\(02\)00757-9](https://doi.org/10.1016/S0167-2738(02)00757-9).
- [59] A. Mahmood, S. Bano, J.H. Yu, K.-H. Lee, High-performance solid oxide electrolysis cell based on ScSZ/GDC (scandia-stabilized zirconia/gadolinium-doped ceria) bi-layered electrolyte and LSCF (lanthanum strontium cobalt ferrite) oxygen electrode, *Energy*. 90, Part 1 (2015) 344–350. <https://doi.org/10.1016/j.energy.2015.06.109>.